Connecting microstructural attributes and permeability from 3D tomographic images of in situ shear-enhanced compaction bands using multiscale computations

WaiChing Sun,[1] José E. Andrade,[1] John W. Rudnicki,[2] and Peter Eichhubl[3]

Received 8 April 2011; revised 12 April 2011; accepted 13 April 2011; published 17 May 2011.

[1] Tomographic images taken inside and outside a compaction band in a field specimen of Aztec sandstone are analyzed by using numerical methods such as graph theory, level sets, and hybrid lattice Boltzmann/finite element techniques. The results reveal approximately an order of magnitude permeability reduction within the compaction band. This is less than the several orders of magnitude reduction measured from hydraulic experiments on compaction bands formed in laboratory experiments and about one order of magnitude less than inferences from two-dimensional images of Aztec sandstone. Geometrical analysis concludes that the elimination of connected pore space and increased tortuosities due to the porosity decrease are the major factors contributing to the permeability reduction. In addition, the multiscale flow simulations also indicate that permeability is fairly isotropic inside and outside the compaction band.
Citation: Sun, W., J. E. Andrade, J. W. Rudnicki, and P. Eichhubl (2011), Connecting microstructural attributes and permeability from 3D tomographic images of in situ shear-enhanced compaction bands using multiscale computations, *Geophys. Res. Lett.*, *38*, L10302, doi:10.1029/2011GL047683.

1. Introduction

[2] Compaction bands are thin tabular zones of localized compactive inelastic deformation and significant porosity reduction. They have been observed in a few field locations, including the upper domain of the Aztec Sandstone at Valley of Fire, Nevada [*Hill*, 1989; *Mollema and Antonellini*, 1996; *Sternlof et al.*, 2004; *Eichhubl et al.*, 2010], and Navajo Sandstone at the Kaibab monocline, Utah [*Solum et al.*, 2010]. Previous research suggested that compaction bands are much less permeable than the host rock and hence could act as barriers to fluid flow. This feature is important to applications involving injection or withdrawal of pore-fluids, such as CO_2 sequestration, energy storage and retrieval, and aquifer management.

[3] In this paper, we use numerical techniques to interpret three-dimensional tomographic images of Aztec sandstone. The cores used here are taken from a band described as a shear-enhanced compaction band (SCB) by *Eichhubl et al.* [2010]. Based on field structural and microtextural observations, they inferred that this band accommodated about equal amounts of shear displacement and band-perpendicular shortening, and distinguished this band from pure compaction bands that lack any component of shear displacement.

[4] Samples were scanned at the synchrotron APS facility in Argonne National Labs as described by *Lenoir et al.* [2010]. The presented techniques afford us unprecedented access to determine grain size distributions, occluded and connected porosities and geometrical tortuosity of samples from the compaction band and the outside matrix. These features are then linked to macroscopic effective permeability tensors using a multiscale lattice Boltzmann/finite element scheme.

[5] *Keehm et al.* [2006] calculated permeabilities from 3D pore geometry statistically reconstructed from 2D images of deformation bands found in the field. A drawback of this approach is that the permeability calculation strongly depends on the quality of pore geometry reconstruction [*Adler*, 1992]. Hence, the accuracy of the permeability calculation can be compromised if the reconstruction from 2D images does not provide realistic three dimensional structures. Alternatively, *Fredrich et al.* [2006] used massively-parallel lattice Boltzmann simulations to extract effective permeability directly from 3D tomographic images of Castlegate sandstone. Permeabilities calculated from the lattice Boltzmann simulations were found by *Fredrich et al.* [2006] to be consistent with laboratory measurements on specimens without deformation bands.

[6] The numerical techniques used here are described in more detail by *Sun et al.* [2011]. They are improved and computationally more efficient versions of those previously used in the literature. An important step to calculate the micro-structural attributes is to obtain the 3D medial axes. *Lindquist et al.* [1996] described constructions of medial axes and used them to determine geometrical tortuosities of several rock types, including a sandstone. Here, we use graph theory and level set-based techniques to calculate 3D medial axes more efficiently.

2. Three-Dimensional Tomographic Images and Numerical Methods

[7] The Aztec Sandstone is a sedimentary rock composed mainly of weakly cemented, well-sorted, well-rounded quartz grains [*Eichhubl et al.*, 2010]. Here, we use tomographic images taken inside and outside a SCB in Aztec sandstone to extract geometrical attributes and effective permeabilities. The converted binary tomographic images used in this study are described by *Lenoir et al.* [2010]. An efficient method to characterize the pore space is to replace it by a structure of medial axes. This method was first used

[1]Division of Engineering and Applied Science, California Institute of Technology, Pasadena, California, USA.
[2]Department of Civil and Environmental Engineering, Northwestern University, Evanston, Illinois, USA.
[3]Bureau of Economic Geology, Jackson School of Geosciences, University of Texas at Austin, Austin, Texas, USA.

0094-8276/11/2011GL047683

by *Lindquist et al.* [1996] to calculate geometrical tortuosity. In their application, medial axes are obtained from the pore space eroded by the discrete BURN algorithm, and Dijkstra's algorithm [*Dijkstra*, 1959] is applied to compute geometrical tortuosity from the medial axes. The discrete BURN algorithm, however, may lead to spurious flow paths that are not medial axes and thus cannot represent the geometry of the pore space efficiently. Moreover, the effective radii of the grains determined by BURN algorithm are not accurate due to the use of integers to store radius data.

[8] To overcome the drawbacks of the BURN algorithm, we use a signed distance function to obtain 3D medial axes [*Sun et al.*, 2011]. The signed distance function $\phi(\vec{x})$ is a continuous metric function measuring the distance between the position $\vec{x}$ and its closest point on the boundary between pore and grain $\vec{y} \in \Gamma$, so that,

$$\phi(\vec{x}) = S(\vec{x}) \inf_{\vec{y}\in\Gamma} \|\vec{x} - \vec{y}\| \tag{1}$$

where inf denotes the infimum and $S(\vec{x})$ is a step function that is equal to -1 if the position $\vec{x}$ is occupied by the solid grains and 1 if $\vec{x}$ is inside pore space. Solving a differential equation by the evolution of a level set function initially taken from the binary image yields the signed distance function. In particular, we use the differential equation formulated by *Li et al.* [2005]. We solve this equation to obtain the signed distance function by introducing an unconditionally stable, semi-implicit 3D level set scheme. More details are given by *Li et al.* [2005] and *Sun et al.* [2011].

[9] According to (1), $\phi(\vec{x})$ reaches its local maximum if $\vec{x}$ is located on the medial axis of the pore space and $\phi(\vec{x})$ reaches its local minimum if $\vec{x}$ is located at the centroid of the solid grains. In the latter case, the value of $\phi(\vec{x})$ is approximately equal to the effective radii of the solid grains, provided that the shapes of the solid grains are well rounded. Since the signed distance function is continuous, the radii determined from it do not need to be integers as in the BURN algorithm. Furthermore, using the signed distance function does not generate spurious flow paths. Since the shortest-path flow channels must be located inside the connected pore space, we identify all voxels inter-connected to the voxels along the shortest flow path as parts of connected pore space and thereby obtain the occluded and connected porosity.

[10] The macroscopic effective permeability is captured by a multiscale hybrid Lattice Boltzmann (LB)/finite element scheme. First introduced to tomographic applications by *White et al.* [2006], this hybrid scheme partitions the specimen into small representative elementary volumes (REV) for LB calculation. Finite element simulations of Darcy's flow are then used to upscale permeabilities of the REV to specimen-scale. This upscaling procedure is the same as used by *White et al.* [2006], but here we conducted LB simulations only on the connected pore space of each REV. This eliminates any chance of mistaking occluded pore space as part of the flow network due to partition of specimens and thus significantly improves the speed and accuracy of the procedure *Sun et al.* [2011].

3. Microstructural Attributes

[11] Using the computational framework described above, we calculate grain size distributions, geometrical tortuosities, and occluded/connected porosities using the 3D signed distance function ϕ (x,y,z) of the tomographic images. Figure 1a depicts the estimated grain size distributions of the samples taken inside and outside the SCB. The average grain diameter is 0.26 mm inside and outside the band, with a variance of 0.013 and 0.021, respectively. Although there are slight differences in the content of fines, both the SCB and outside matrix display well sorted grains of similar sizes. This similarity in grain sizes may be explained by the partially cemented microfractures produced during band formation, which may offset the higher degree of grain breakages observed inside the bands, as shown in Figures 1c and 1d. Furthermore, the average grain volume (1.6×10^7 μm^3) is five orders of magnitude larger than that of the tomographic image voxel (216 μm^3), suggesting that the tomographic images have enough resolution to render the grain geometry accurately.

[12] Figures 2a and 2b show the shortest flow paths for $0.6 \times 0.6 \times 0.6$ mm^3 Aztec sandstone specimens from inside and outside the SCB. As illustrated, the pore space is much less interconnected and has fewer flow channels inside the band than in the host rock. The flow channels inside and outside the band are both highly three dimensional, suggesting that reconstructions from two dimensional slices may not give an accurate picture.

[13] Next, we calculate geometrical tortuosities of larger specimens, $2.25 \times 2.25 \times 6$ mm^3, that contain sufficient flow channels to be statistically representative. Geometrical tortuosity τ is defined as the ratio between the length of the actual flow path l and the linear separation between two parallel planes d, i.e., $\tau = l/d$ [*Adler*, 1992; *Lindquist et al.*, 1996]. Figure 1b illustrates the distribution of geometrical tortuosities inside and outside the SCB. The mean value is 2.5 inside the band and 2.0 outside. More specifically, more than 30% of the flow channels in the band have geometrical tortuosities greater than 2.8, while less than 1% of flow channels in the outside matrix have tortuosities greater than 2.8. These results quantitatively demonstrate that the grain re-arrangement and pore collapse inside the band lead to significantly more tortuous flow channels. Consequently, flow within the band is more difficult. The distribution of geometrical tortuosity, both inside and outside the band, is fit well by the Gamma distribution (Figure 1b), as noted by *Lindquist et al.* [1996] for Berea sandstone. The variance of the geometrical tortuosity is 0.18 inside and 0.06 outside the SCB indicating a much wider distribution of the lengths of flow channels inside the band.

[14] From the tomographic images, we calculate an average total porosity of 20% inside the band and 14% outside. These results are consistent with other measurements in Aztec sandstone by *Eichhubl et al.* [2010] and *Sternlof et al.* [2004]. However, we are able to calculate not only the total porosity but also the occluded and connected porosities. The occluded (connected) porosity is the total volume of the occluded (connected) pore space divided by the total volume of both pore space and solid grains. The sum of the occluded and connected porosities is equal to the total porosity.

[15] Figure 3 depicts the occluded and connected porosities of 6 cubic samples, 3 from the shear enhanced compaction band (labeled as SCB) and 3 from the outside matrix (labeled as OUTSIDE). The side lengths are all 0.75 mm. As illustrated in Figure 3, three equally spaced samples traverse

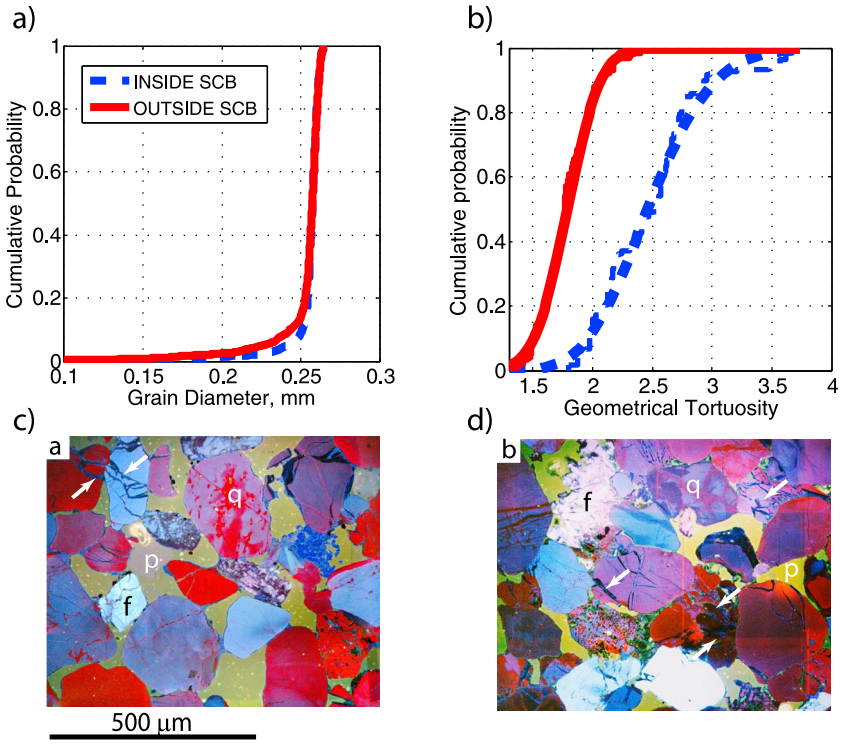

Figure 1. Cumulative distribution functions of (a) grain diameters and (b) geometrical tortuosities and Scanning-electron microscope cathodoluminescent images (c) outside and (d) inside the shear enhanced compaction band. Thick lines in Figure 1b denote Gamma distribution fits; thin lines represent the geometrical tortuosity distributions determined from Dijkstra's algorithm. In Figures 1c and 1d, q:quartz, p:pore. Arrow indicates quartz cement in broken grains.

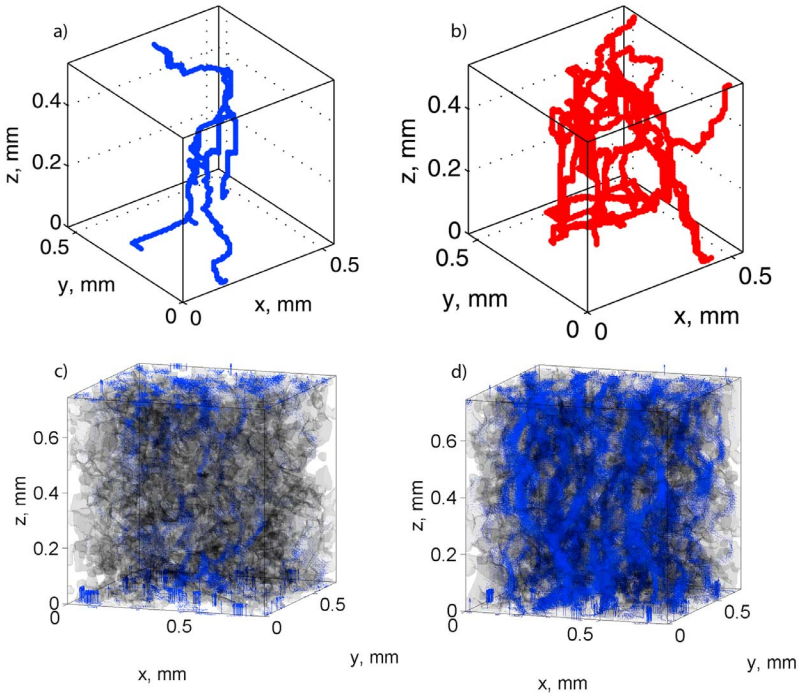

Figure 2. The shortest flow paths (a) inside and (b) outside and velocity vector field (in blue color) (c) inside and (d) outside the shear enhanced compaction band. Solid grains are colored in gray. The intensity of the blue color in Figures 2c and 2d represents the magnitude of the fluid velocity field.

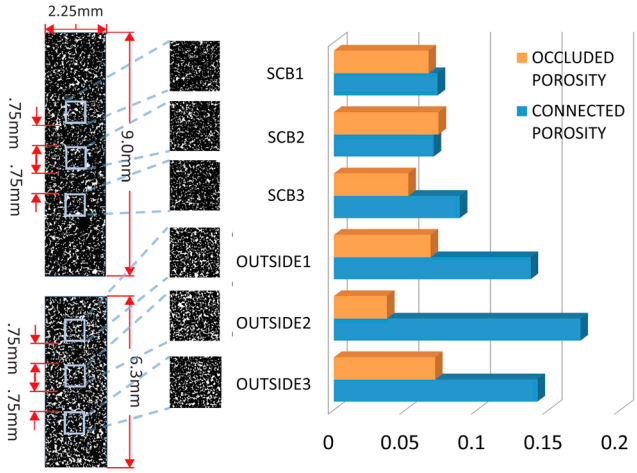

Figure 3. Occluded and connected porosity of 6 samples taken inside/outside the shear enhanced compaction band in the Aztec Sandstone specimen. Sample labeled as SCB (OUTSIDE) are taken inside (outside) the shear enhanced compaction band.

the width of the SCB, about 1 cm. They are taken from images between 3.66 mm and 6.66 mm beneath the top band boundary. The other three samples are from outside the band at successively larger distances from the band boundary. The occluded porosity is about the same, an average of 5.8% for specimens inside the band and 6.4% for those outside. The 7.7% connected porosity inside the band is only roughly half of the 15% connected porosity outside. Thus, the reduction occurs primarily in the connected porosity which contributes to the formation of a flow barrier.

4. Macroscopic Effective Permeabilities

[16] The directional permeabilities of two hundred 0.75 × 0.75 × 0.75 mm^3 samples (half inside, half outside the band) are calculated via lattice Boltzmann simulations. The volume of the samples is selected based on an energy dissipation criterion proposed by *Sun et al.* [2011] to minimize size effects and obtain representative permeability calculations. We estimate an average permeability of 2.1×10^{-13} m^2 inside the band and 1.3×10^{-12} m^2 outside, and a variance of 0.26 and 0.18, respectively. The increase on the ratio between standard deviation and mean value signifies that the pore geometry of the band is less homogeneous than the outside matrix. The macroscopic effective permeabilities of two 2.25 mm × 2.25 mm × 6 mm samples are determined via a lattice Boltzmann/finite element scheme [*White et al.*, 2006; *Sun et al.* 2011]. Figures 2c and 2d show the magnitude of the velocity field generated from the lattice Boltzmann method by imposing a pore pressure gradient on two opposite faces of the samples. The solid grains are plotted in gray color whereas the blue shaded region represents occurrence of fluid flow. Higher intensity of the blue color indicates higher fluid flux. Figures 2c and 2d confirm that fluid flow inside a SCB is confined to only a small portion of the entire pore space, whereas the fluid flow in the outside matrix distributes more evenly over the specimen. This finding is consistent with the higher connected/occluded porosity ratio inside SCB. The effective permeability is obtained according to,

$$k_{ij} = -\frac{\mu^v}{p_{,j}} \frac{1}{V_\Omega} \int_\Omega v_i(\vec{x}) d\Omega \tag{2}$$

where μ^v is the dynamic viscosity of the fluid occupying the spatial domain of the porous medium Ω.

[17] The effective permeabilities reported above based on lattice Boltzmann/finite element simulations, pertain to the direction normal to the SCB. The 0.77 order of magnitude difference is close to the 1.1 order permeability reduction predicted from the modified Kozeny-Carman equation [*Carman*, 1956] using connected porosities ϕ^f, which reads

$$\frac{k_{in}}{k_{out}} = \frac{\tau_{out}}{\tau_{in}} \left(\frac{\phi^f_{in}}{\phi^f_{out}} \right)^3 \left(\frac{1-\phi^f_{out}}{1-\phi^f_{in}} \right)^2 \tag{3}$$

Nevertheless, the effective permeability reduction obtained from multiscale simulations and the modified Kozeny-Carman equation are both less than the several orders of magnitude inferred for compaction bands in laboratory sandstone specimens [*Holcomb and Olsson*, 2003; *Vajdova et al.*, 2004] and the 2.5 order of magnitude permeability reductions inferred by *Keehm et al.* [2006]. Presumably, the larger permeability reduction for the laboratory specimens is due to more intense comminution in lab specimens compared to compaction bands collected in the field (see Figures 1c and 1d). The estimates of *Keehm et al.* [2006], and similar estimates by *Solum et al.* [2010] are based on pore volume reconstructions from two-dimensional images. As mentioned earlier, this seems likely to overestimate the reduction in permeability. Whether the difference in methodology is sufficient to account for the order of magnitude difference is unclear but illustrates the need for further studies of this type.

[18] The procedure used here also makes it possible to estimate the permeability parallel to the band. We find that the permeability in this direction is roughly the same as parallel to the band, with a 0.74 reduction of effective permeability along the axis parallel to the band. This nearly isotropic transport property is consistent with the orientation of maximum compressive principal stress (45–50 degree to the bands) inferred by *Eichhubl et al.* [2010] based on field structural and microtextural observations. Furthermore, the results suggest that reduction of connected pore space and increases of geometrical tortuosities also decrease permeability parallel to the band. These mechanisms seem to be less likely, than, for example, grain crushing and comminution to have a strong directional dependence. This is an important issue since deformation bands that have experienced relatively large shear (compared with compaction) may develop through-going slip surfaces. This could increase the permeability in that direction and create a preferential flow paths.

5. Conclusion

[19] Using a computationally efficient method, we compare macroscopic permeabilities and microstructural attributes of a shear-enhanced compaction band and host rock. Our results reveal that increased tortuosity and elimination of connected pore space, not simply a reduction in total porosity, are the major factors causing reduced permeability. Furthermore, the results suggest that permeability is reduced

not only for flow perpendicular to the band but also for flow along the band.

[20] **Acknowledgments.** This research has been partly funded by the Geoscience Research Program of the U.S. Department of Energy under grant DE-FG02-08ER15980. This support is gratefully acknowledged. We thank Nicolas Lenoir for providing the tomographic images of the Aztec Sandstone. We are also very grateful to Aaron Packman and Cheng Chen for valuable discussion on the lattice Boltzmann method. PE acknowledges John Hooker for assistance with SEM imaging, and the FRAC industrial consortium for financial support.

References

Adler, P. M. (1992), *Porous Media: Geometry and Transport*, *Butterworth-Heinemann Ser. Chem. Eng.*, Butterworth-Heinemann, Stoneham, Mass.

Carman, P. C. (1956), *Flow of Gases Through Porous Media*, Butterworth Sci., London.

Dijkstra, E. W. (1959), A note on two problems in connexion with graphs, *Numer. Math.*, *1*, 269–271.

Eichhubl, P., J. N. Hooker, and S. E. Laubach (2010), Pure and shear-enhanced compaction bands in Aztec Sandstone, *J. Struct. Geol.*, *32*, 1873–1886.

Fredrich, J. T., A. A. DiGiovanni, and D. R. Noble (2006), Predicting macroscopic transport properties using microscopic image data, *J. Geophys. Res.*, *111*, B03201, doi:10.1029/2005JB003774.

Hill, R. E. (1989), Analysis of deformation bands in Aztec Sandstone, Valley of Fire State Park, Nevada, M.S. thesis, 68 pp., Univ. of Nev., Las Vegas.

Holcomb, D. J., and W. A. Olsson (2003), Compaction localization and fluid flow, *J. Geophys. Res.*, *108*(B6), 2290, doi:10.1029/2001JB000813.

Mollema, P. N., and M. A. Antonellini (1996), Compaction bands: A structural analog for anti-mode I cracks in aeolian sandstone, *Tectonophysics*, *267*, 209–228.

Keehm, Y., K. Sternlof, and T. Mukerji (2006), Computational estimation of compaction band permeability in sandstone, *Geosci. J.*, *10*(4), 409–505.

Lenoir, N., J. E. Andrade, W. C. Sun, and J. W. Rudnicki (2010), In situ permeability measurements inside compaction bands using X-ray CT and lattice Boltzmann calculations, in *Advances in Computed Tomography for Geomaterials: GeoX2010*, edited by K. A. Aishibli and A. H. Reed, pp. 279–286, John Wiley, Hoboken, N. J.

Li, C., C. Xu, C. Gui, and M. D. Fox (2005), Level set evolution without re-initialization: A new variational formulation, in *Proceedings of 2005 IEEE Computer Society Conference on Computer Vision and Pattern Recognition (CVPR 2005)*, pp. 430–436, IEEE Comput. Soc., Los Alamitos, Calif.

Lindquist, W., S.-M. Lee, D. Coker, K. Jones, and P. Spanne (1996), Medial axis analysis of void structure in three-dimensional tomographic images of porous media, *J. Geophys. Res.*, *101*(B4), 8297–8310.

Solum, J. G., J. P. Brandenburg, S. J. Naruk, O. V. Kostenko, S. J. Wilkins, and R. A. Schultz (2010), Characterization of deformation bands associated with normal and reverse stress states in the Navajo Sandstone, Utah, *AAPG Bull.*, *94*, 1453–1475.

Sternlof, K. R., J. R. Chapin, D. D. Pollard, and L. J. Durlofsky (2004), Permeability effects of deformation band arrays in sandstone, *AAPG Bull.*, *88*, 1315–1329.

Sun, W. C., J. E. Andrade, and J. W. Rudnicki (2011), Multiscale method for characterization of porous microstructures and their impact on macroscopic effective permeability, *Int. J. Numer. Methods Eng.*, doi:10.1002/nme.3220, in press.

Vajdova, V., P. Baud, and T. Wong (2004), Permeability evolution during localized deformation in Bentheim sandstone, *J. Geophys. Res.*, *109*, B10406, doi:10.1029/2003JB002942.

White, J. A., R. I. Borja, and J. T. Fredrich (2006), Calculating the effective permeability of sandstone with multiscale lattice Boltzmann/finite element simulations, *Acta Geotech.*, *1*, 195–209.

J. E. Andrade and W. C. Sun, Division of Engineering and Applied Science, California Institute of Technology, 1200 E. California Blvd., Pasadena, CA 91125, USA. (jandrade@caltech.edu)

P. Eichhubl, Bureau of Economic Geology, Jackson School of Geosciences, University of Texas at Austin, Austin, TX 78713, USA.

J. W. Rudnicki, Department of Civil and Environmental Engineering, Northwestern University, 2145 Sheridan Rd., Evanston, IL 60208, USA.